



Cite this: *Nanoscale Adv.*, 2022, **4**, 3537

## Quantification and removal of carbonaceous impurities in a surfactant-assisted carbon nanotube dispersion and its implication on electronic properties†

Minsuk Park, In-Seung Choi and Sang-Yong Ju  \*

Carbonaceous impurities (CIs) affect the optoelectronic properties as well as the ability to use absorption spectroscopy to estimate the metallic content of a single-walled carbon nanotube (SWNT) dispersion. Therefore, a method for the accurate quantification and removal of CIs is required. We have devised methods to characterize and quantify CIs present in SWNT batches and to determine the effects of CIs on the optical and electrical properties of SWNT. Quantitative determination of CIs stems from the finding that chloroform selectively disperses CIs present in SWNT batches. CIs separated by dispersing the as-purchased SWNT batch in chloroform have the morphology of defective and agglomerated few-layered graphenes, whose sizes and locations depend on SWNT batches. Moreover, CIs exhibit a featureless UV-vis-mid-wavelength IR (MWIR) absorption curve and an extinction coefficient comparable to graphenes and show difference with carbon black, which is frequently used as the CI reference. The MWIR region that shows least absorptions caused by the transition of various SWNT types was utilized to assess the significant contribution made by CIs present in a surfactant-assisted SWNT dispersion, showing about 12–19 wt% of CIs in various SWNT dispersions. In addition, the extraction of CIs with chloroform results in a highly purified SWNT batch without any diameter distribution change originating from oxidative damage as compared to the commercially available purified SWNT batch. Finally, we found that increasing the weight of CIs present in a SWNT dispersion strongly lowers the thermal conductivity of a SWNT film when compared with the electrical conductivity. This study provides a way to understand the negative effects that CI has on the optoelectronic properties of SWNTs as well as the beneficial effects of excluding ubiquitous CIs in SWNTs batches.

Received 12th March 2022  
Accepted 10th June 2022

DOI: 10.1039/d2na00153e  
[rsc.li/nanoscale-advances](http://rsc.li/nanoscale-advances)



Department of Chemistry, Yonsei University, 50 Yonsei-ro, Seodaemun-Gu, Seoul 03722, Republic of Korea. E-mail: [syju@yonsei.ac.kr](mailto:syju@yonsei.ac.kr); Tel: +82-2-2123-5639

† Electronic supplementary information (ESI) available: Absorption cross section calculation of monolayer graphene, defect density calculations of CI and CB, assignment of FT-IR bands absorption spectra comparison of CI, UV-vis-MWIR absorption spectrum of CI containing chloroform dispersion (Fig. S1), absorption spectra comparison of CI dispersion in chloroform, CB, and graphene (Fig. S2), TEM and SEM images of CI dispersion in chloroform (Fig. S3), CI-subtracted absorption spectrum of FC12-PSWNT dispersion (Fig. S4), UV-vis-FIR absorption spectra of FC12 dispersions in *p*-xylene (Fig. S5), AFM height images of acetone-washed HiPco, PSWNT, and LDSWNT (Fig. S6), absorption spectra of vigorous chloroform dispersions (Fig. S7), atomic contents of PSWNT, acetone-washed PSWNT and CI (Fig. S8), TGA thermograms (Fig. S9), overall wt. including CI/SWNT and net SWNT purity (Fig. S10), overlaid CI-subtracted net PSWNT spectra (Fig. S11), comparison of AFM-based number of CI per SWNT length (Fig. S12), configuration of prepatterned chip for  $\sigma$  and  $\kappa$  measurements (Fig. S13), photographs of the transferred PSWNT films on prepatterned chips (Fig. S14), CI-added FC12-PSWNT dispersions (Fig. S15) and thickness changes of PSWNT film on a quartz substrate by a surface profiler (Fig. S16) are provided. This material is available free of charge via the Internet. See <https://doi.org/10.1039/d2na00153e>

## 1. Introduction

Single-walled carbon nanotubes (SWNTs) with defined electrical properties are optimal materials for next-generation optoelectronic devices. Semiconducting (*s*)-SWNTs are especially interesting because they have excellent electrical properties including high current on/off ratios exceeding  $10^6$  and charge carrier mobility.<sup>1–5</sup> Owing to their unique features, *s*-SWNTs have broad solution-based applications in thin film transistors,<sup>1–5</sup> thermoelectric devices,<sup>6–8</sup> and photovoltaic devices.<sup>9–11</sup> The SWNT batch contains SWNTs, carbonaceous impurities (CIs) and metal catalysts, among which the metal catalysts possessing metals inside graphitic shells can be easily removed by centrifugation owing to their density.<sup>16</sup> Despite these potential impacts, SWNTs suffer from heterogeneity issues associated with the presence of CIs<sup>12,13</sup> formed as byproducts during SWNT growth and serves as an obstacle for high-end optoelectronic applications.

The CI has a metallic property originating from the graphitic structure of several layers with a size of several tens of nanometers. These structural characteristics promote the adsorption

of CIs onto the surface of SWNTs, which form aggregates themselves, making it difficult to distinguish them from SWNTs.<sup>14,15</sup> In particular, metallic CIs act as scatters for electric charge conduction and heat transfer through SWNTs, thereby lowering intrinsic properties<sup>15</sup> and interfering with SWNT signals in electrochemical reactions.<sup>16</sup> For this reason, many efforts are made to remove CIs, and one of them is the method of removing CIs *via* oxidation. However, this removal method makes the price several orders of magnitude more expensive<sup>17</sup> and has the disadvantage of generating oxidation defects<sup>18</sup> by reacting structurally similar SWNTs.

With the development of the technology for separating *s*-SWNTs from the dispersion phase,<sup>19–22</sup> the analysis method for CIs present in the solution phase is also an important factor in making pure *s*-SWNTs. Among various CI analysis methods,<sup>23–25</sup> the absorption of the CI is thought to be the most suitable method for its quantification since the metallic nature of the CI is expected to be featureless absorption, which is clear departure from the absorption peak form resulting from one-dimensional van Hove singularity (vHs) of SWNTs. However, since there is no method to selectively extract only CIs from SWNTs, carbon black (CB) that has a globular graphitic structure is used to define the background absorption instead, leading to large variations. Especially, a greater deviation occurs while quantifying impurities in *s*-enriched SWNT dispersions with a high purity of 90% or more. For this reason, purity evaluation methods of *s*-SWNTs using Raman mapping<sup>26</sup> or thin film transistors<sup>27</sup> have been proposed. Therefore, there is a need for a method capable of precisely analyzing the content of CIs in the SWNT dispersion in the solution phase.

In the study described below, we developed a method for the quantification of CIs in a SWNT dispersion. The properties of the CI were characterized by various methods including absorption spectroscopy, transmission electron microscopy (TEM), scanning electron microscopy (SEM) and Raman spectroscopy. The effect of the CI on an SWNT dispersion prepared using a *N*-dodecyl flavin surfactant (FC12) was investigated by UV-vis-mid-wavelength IR (MWIR) absorption spectroscopy. Furthermore, we observed that chloroform can be employed to disperse only the CI component in the as-prepared SWNT, leaving the pure SWNT as a precipitate, and the degree of CI extraction depends on its morphology. This selected dispersion technique provides a framework for deconvoluting contributions by CIs to the absorption spectrum, gravimetric and thermal analysis, and purity of the as-prepared SWNT. The CI-excluded absorption spectrum displays net optical transitions of *s*- and metallic (*m*)-SWNT over the entire absorption region. Moreover, we were able to measure the extinction spectrum of CIs, which should be of use to workers in the field. Finally, the effects of the CI on the properties of the SWNT were investigated using electrical conductivity ( $\sigma$ ) and thermal conductivity ( $\kappa$ ).

## 2. Methods

### 2.1. Materials and instrumentation

Two SWNT batches with different CI contents were utilized: plasma-torch-grown SWNTs termed PSWNTs (RN-220 SWCNTs,

batch# R26-036, nanotube purity of >70%, NanoIntegris, Canada) and super purified PSWNTs termed SPSWNTs (SPT-220 SWCNT, batch# PL32-059, nanotube purity of 95–99%, NanoIntegris, Canada). Their SWNT diameter ( $d_t$ ) distribution is  $1.3 \pm 0.35$  nm. SWNTs with different average  $d_t$  are high-pressure carbon monoxide (HiPco) process-generated SWNTs ( $d_t$  distribution:  $1.0 \pm 0.35$  nm, Raw grade, batch #: HR35-067, minimum SWNT contents > 65%, NanoIntegris, Canada) and larger  $d_t$  SWNTs (LDSWNTs,  $d_t$  distribution < 3.0 nm, CAS #: 308 068-56-6, TCI, Japan). Measurements were carried out at room temperature unless otherwise noted. Gravimetric analyses of CIs and SWNT were made using a high-precision balance (0.01 mg precision, NewClassic MS, Mettler Toledo, OH, USA).

**2.1.1. TEM measurements.** TEM measurements were conducted using a Tecnai G<sup>2</sup> F30ST (FEI company, OR, USA) operating at an accelerating voltage of 300 kV. For TEM measurements, copper TEM grids covered with an ultrathin carbon support (LC200-Cu, lot no.: 180 912, 200 mesh, TED Pella, USA) were floated in an upside-down manner on the top of a drop of nanomaterial dispersion on a glass slide substrate. To adjust the sample concentration on the TEM grid, the sample-adsorbed grid was washed with drops of a pure dispersion solvent. After the dilution step, the grid was dried under vacuum overnight.

**2.1.2. Absorption measurements.** UV-vis-MWIR absorption spectra up to 3200 nm were recorded using a JASCO V-770 (Japan) using absorption cuvettes having a 1 mm path length (21/Q/1, Starna scientific, UK). Absorbances were measured *via* a double-beam configuration. UV-vis regions are dispersed by 1200 lines per mm grating and the MWIR region is dispersed by 300 lines per mm grating.  $D_2$  and halogen lamps were used for excitation at 190 to 350 nm and 330 nm to 3200 nm, respectively. The wavelength accuracy was 0.3 nm for UV-vis and 1.5 nm for MWIR regions. The photometric accuracy is 0.0015 Abs for 0 to 0.5 Abs, and 0.0025 Abs for 0.5 to 1 Abs. Detectors for UV-vis and NIR regions were photomultiplier tubes and PbS photoconductive cells.

**2.1.3. FT-IR measurements.** The spectra were acquired using a Jasco FT-IR 4700 spectrophotometer in the range of 400 to  $4000\text{ cm}^{-1}$ . The spectra were accumulated 32 times. The SWNT dispersions were introduced to a liquid sample cell (Barnes demountable liquid cell kit, beam path length: 1 mm, KBr crystal). Precaution was taken to exclude air bubbles in the cell. The spectra were stitched in the 2900–3200 nm region of the absorption spectra recorded using a UV-vis-MWIR absorption spectrometer.

**2.1.4. Resonance Raman spectroscopy measurements.** Raman spectra were recorded using a custom-made setup<sup>28</sup> with a 532 nm laser (Cobolt, Hübner Photonics, Germany) with 0.1 mW power and a 50 $\times$  objective lens (MPlan, NA = 0.75) *via* a backscattering geometry and were calibrated using the Si peak ( $520.89\text{ cm}^{-1}$ ) as the internal reference.

**2.1.5. SEM measurements.** SEM measurements were conducted using Schottky emission SEM (SU-70, Hitachi, Japan) operating at an accelerating voltage of 10 kV. SEM images of SWNT films were obtained at a working distance of *ca.* 11 mm



under the condition of 100 k magnification. All measurements were conducted without any conductive metal coating.

**2.1.6. Atomic force microscope (AFM) measurements.** AFM measurements were conducted using a commercially available AFM (NX10, Park systems, Republic of Korea). An Al-coated silicon cantilever with a spring constant of  $37\text{ N m}^{-1}$ , a resonance frequency of 300 kHz, and quoted radius of *ca.* 6 nm (ACTA, App Nano, USA) was utilized to measure height topographies. Typically, a  $512 \times 512$  pixel image was collected from  $5\text{ }\mu\text{m} \times 5\text{ }\mu\text{m}$  area. Prior to AFM measurements, SWNTs with various  $d_t$  were deposited onto 285 nm-thick  $\text{SiO}_2/\text{Si}$  substrates by dipping into the SWNT dispersion for 30 min. Then, the substrate was rinsed several times with fresh methanol and dipped into fresh methanol to remove residual flavin completely. After that, the rinsed substrate was dried under a  $\text{N}_2$  flow. In the case of SPSWNTs, 200  $\mu\text{L}$  of dispersion was drop-casted onto a substrate. After 10 min, the substrate was rinsed several times with a fresh methanol until no green fluorescence originating from flavin derivatives was observed using a hand-held UV lamp (*i.e.*, 365 nm). The measured height topographies were analyzed using XEI 4.3.4 program (Park systems, Republic of Korea).

**2.1.7. X-ray photoelectron spectroscopy (XPS).** XPS spectra were recorded using a Nexsa XPS System (Thermo Fisher Scientific, USA). The spot size of irradiation is *ca.* 400  $\mu\text{m}$  and the binding energy position was calibrated by  $\text{C}_{1s}$  position as 284.8 eV.

**2.1.8. Thermogravimetric analysis (TGA).** TGA measurements were conducted using a TGA Q500 (TA Instruments, USA). For this purpose, *ca.* 3 mg of nano carbon film or powder was used. Sample heating was ranged from room temperature to 900  $^{\circ}\text{C}$  at a ramping rate of  $10\text{ }^{\circ}\text{C min}^{-1}$  under a 100 standard cubic centimeter per minute flow of synthetic air composed of 21 vol%  $\text{O}_2$  and 78% of  $\text{N}_2$ .

## 2.2. Construction of Kataura plot

Since the surfactant-based SWNT dispersions were utilized, the Kataura plot was constructed based on the empirical equation of optical transitions from sodium dodecyl sulfate (SDS)-dispersed SWNTs for *s*-SWNTs<sup>29</sup> and Rayleigh scattering for *m*-SWNTs.<sup>30</sup> For *s*-SWNTs, SDS-SWNTs were adopted to have the closest match with the flavin surfactant system.<sup>31</sup> On the contrary, optical transitions of *m*-SWNTs were obtained from the suspended tube in a trench since excitonic effects on *m*-SWNT<sup>32</sup> are negligible as compared to *s*-SWNTs.<sup>33</sup>

## 2.3. CI-enriched dispersions

The as-purchased PSWNTs (1 mg) were added to 4 mL of chloroform, which was dried over 3  $\text{\AA}$  molecular sieve (Alfa Aesar, MA, USA) overnight prior to use. The resulting mixture was subjected to brief bath sonication (20 min, Branson 1510, 70 W, Emerson, USA) and centrifugation at 10 kg for 10 min using a high-performance centrifuge with a fixed angle rotor (Avanti J-26 XPI and JA-25.50, respectively, Beckman Coulter, IN, USA) at room temperature using an organic solvent-tolerant centrifugal tube (50 mL, Cat. #: 3114-0050, fluorinated poly(ethylene)-co-

poly(propylene), Nalgene, USA). After centrifugation, the 70% supernatant was collected for use in further measurements. Repetitive CI extractions were conducted in a similar way. The extraction of CIs from the HiPeo and LDSWNTs requires more vigorous sonication owing to the tightly adsorbed CI on SWNTs. Then, 1 mg of as-purchased SWNTs were added to 1 mL of chloroform (instead of 4 mL for PSWNTs). After brief bath sonication for 20 min, the resulting mixture was subjected to 5 h tip sonication (40% power, 25  $\text{W mL}^{-1}$ , probe tip diameter: 13 mm, VCX 750, Sonics & Materials, USA) with a bath temperature of 15  $^{\circ}\text{C}$  maintained by an external water circulator (Lab Companion RW-2025G, Jeio Tech, Republic of Korea). Then, centrifugation at 10 kg for 30 min was conducted and 70% supernatant was collected. Prior to AFM measurements, the CI was deposited on  $\text{SiO}_2/\text{Si}$  substrates by dipping into the CI-enriched chloroform dispersion for 30 min. Then, the substrate was rinsed with fresh chloroform and dried under a  $\text{N}_2$  flow.

## 2.4. SWNT dispersions

A mixture of 1 mg of PSWNT and 1 mg of FC12 was added to 4 mL of *p*-xylene, which was dried over a 3  $\text{\AA}$  molecular sieve overnight prior to use. The resulting mixture was subjected to brief bath sonication for mixing, and then to 1 h tip sonication (18.8  $\text{W mL}^{-1}$ ). Centrifugations at 5 kg were conducted for 2 h and the 80% supernatant was collected for use in further measurements. Sonication and centrifugation were conducted with the aforementioned equipment for CI extraction. Surfactant-free SWNT dispersion was prepared by addition of 1 mg of as-prepared PSWNTs to 4 mL of *N*-methyl pyrrolidone (NMP) with brief bath sonication (1 h). The as-sonicated NMP dispersion was used directly for TEM sampling without any centrifugation. SWNT dispersions with different  $d_t$ , CI-removed PSWNT dispersions, and SPSWNT dispersions were obtained by using FC12 with a similar protocol. An *m*-enriched FC12-PSWNT dispersion was prepared by re-dispersion of the precipitate according to our previous work.<sup>5</sup>

## 2.5. SWNT film preparation

An acetone-dissolvable membrane filter was used to prepare PSWNT films on a quartz substrate. A 0.1  $\mu\text{m}$  pore-size mixed cellulose ester membrane filter (1" in diameter, cat. #: A010A025A, Advantec, Japan) was used to filter *ca.* 3 mL of PSWNT dispersion for further use. To prepare the SWNT film, the membrane filter was placed in upside-down manner on a quartz substrate (2.5 cm  $\times$  2.5 cm  $\times$  1 mm, NC-200, Hanjin Quartz, Republic of Korea) having 20  $\mu\text{L}$  of deionized water droplet to promote better adhesion. A dummy top slide glass was placed and pressurized on the top of the membrane filter/SWNT film for few seconds to promote even adherence of the membrane filter on SWNTs. After the dummy slide glass was removed, the entrapped DI water was carefully removed using a tissue wiper along the perimeter of the membrane filter, and the membrane-adhered quartz substrate was quickly loaded into a custom-made acetone vapor reflux chamber prior to dryness. Special care was taken in placing the quartz substrate,



so it does not come in direct contact with the acetone drop condensed by a reflux condenser. The dissolution of the membrane filter can be observed by melting out a whitish membrane residue within few hours and the complete removal time required is two days. The average thickness of each PSWNT film was measured more than five times using a surface profiler (Dektak XT, Bruker, USA) for  $\sigma$  and  $\kappa$  analyses.

## 2.6. Deterministic transfer of SWNT films to a prepatterned device

The PSWNT film transfer process was adopted from a poly(methyl methacrylate) (PMMA)-assisted graphene transfer method.<sup>28,34</sup> Deterministic transfer of thin SWNT films follows the previous protocol.<sup>35</sup> In order to transfer the SWNT film on a quartz substrate to a prepatterned chip, a PSWNT film-placed quartz substrate was initially spin-coated with PMMA (molecular weight: 950 kDa, 2% dilution in anisole (A2), MicroChem, MA, USA) at 1000 rpm for 60 s (SF-1A, BGK, Republic of Korea). After that, a PMMA-coated PSWNT film was cut carefully using a sharp blade to make the rectangular film (5 mm  $\times$  3 mm size), which fits on the desired area of the pre-patterned chip. The PMMA-coated PSWNT film was carefully detached from a quartz substrate by floating on a buffered oxide etchant (10 : 1 volume ratio, 36% of NH<sub>4</sub>F and 4.7% of HF, etching rate: 1 nm s<sup>-1</sup> at 25 °C, Sigma-Aldrich, MO, USA) for 2 h. The floated PSWNT film with the PMMA coating was scooped out using a clean slide glass and washed with residual oxide etchant and subsequently with DI water two times. The rectangular PSWNT film

was transferred to an exact position of a pre-patterned chip (lithographically defined Pt electrodes (100 nm) on a 300  $\mu$ m-thick (100) Si substrate with a suspended Si<sub>3</sub>N<sub>4</sub> layer (100 nm) and an Al<sub>2</sub>O<sub>3</sub> passivation layer (30 nm))<sup>36</sup> via a custom-made *x*-*y*-*z* transfer system described in our previous report.<sup>35</sup> To remove the PMMA coating on the PSWNT film, the chip was immersed in a clean acetone bath overnight and dried at 90 °C under 10<sup>-3</sup> torr vacuum.

## 2.7. $\sigma$ and $\kappa$ measurements

Both  $\sigma$  and  $\kappa$  measurements were conducted using a thin film analyzer (TFA, Linseis, Germany) based on a previous report.<sup>36</sup>  $\sigma$  was measured by the 4-point van der Pauw method using the determined thickness.  $\kappa$  was obtained by the  $3\omega$  method to correct for the thermal conductivities of the 100 nm-thick Si<sub>3</sub>N<sub>4</sub> layer and the Al<sub>2</sub>O<sub>3</sub> passivation layer. All measurements were conducted under high vacuum up to 7.5  $\times$  10<sup>-6</sup> torr.

## 3. Results and discussion

In the first phase of this investigation, the morphologies of the components of as-purchased PSWNTs were explored. The quoted contents of the PSWNT are 85–90% SWNTs and CIs, and 10–15% of a trace metal catalyst.<sup>17</sup> The morphology of this material, dispersed in NMP using 1 h bath sonication, was investigated by TEM. The TEM image in Fig. 1A shows that the sample comprises bundled SWNTs and nearby CI particles, suggesting that a strong interaction exists between equal

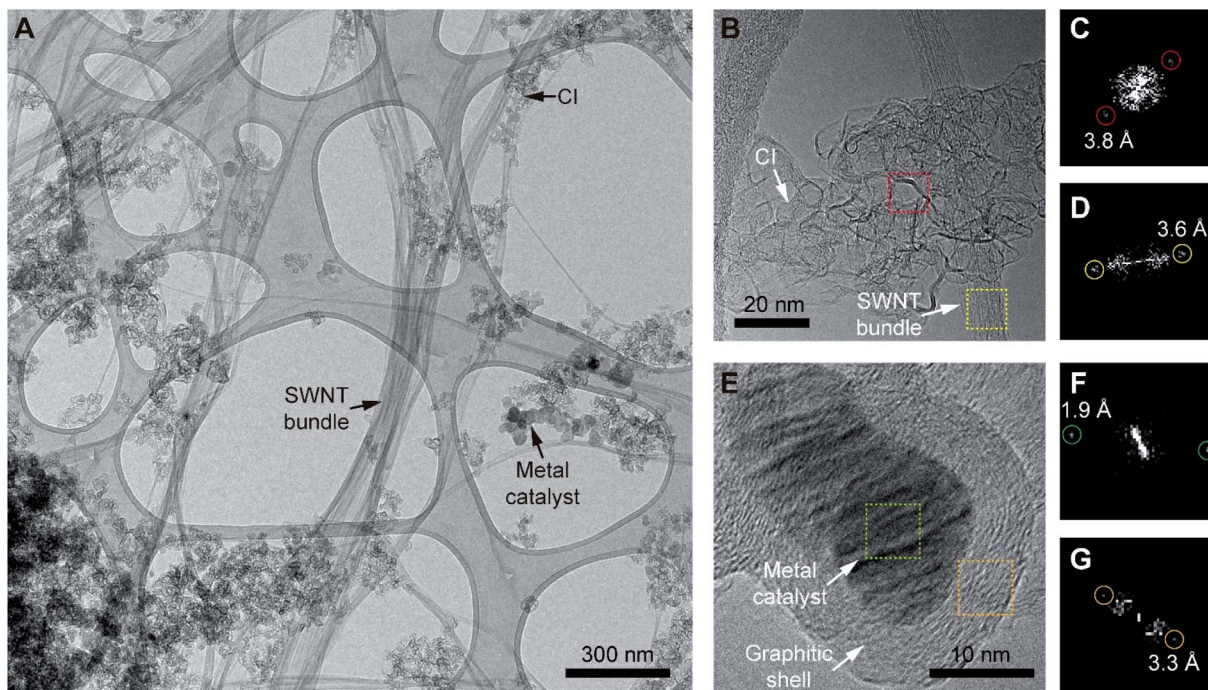


Fig. 1 Morphologies of components in the as-purchased PSWNT, which were obtained by TEM on a sample prepared using a sonication-assisted NMP dispersion. TEM images of (A) SWNT, CI, and metal catalyst, (B) CI agglomerates near the SWNT bundle and (E) metal catalysts covered by graphitic shells. FFT images of (C) CI and (D) bundled SWNT regions obtained from boxes in (B). FFT images of (F) metal catalyst and (G) graphitic shell regions obtained from boxes in (E).



graphitic sidewalls of the two components. The magnified view in Fig. 1B shows that the CI exists in a disk-like agglomerated form with edge-scrolled, crumpled flakes with a size of 10–20 nm. Moreover, fast Fourier transform (FFT) image of the scrolled area (Fig. 1C) shows the presence of a few-layered graphene structure with a layer spacing of 0.38 nm. This result indicates that the CI has a defect containing few-layered graphene structures, which contrasts with that of highly crystalline graphite that has a vdW distance of 0.34 nm and bundled PSWNT that has 0.36 nm spacing between the tubes (see FFT image of Fig. 1D). In addition, the morphology of the CI is different from that of CB, which has an onion-like graphitic shell structure and a large number of  $sp^3$  carbons.<sup>37</sup>

As compared to the CI whose inner part is empty, the metal catalyst comprised of Ni, Fe, and Co<sup>17,38–40</sup> (Fig. 1E) has a comparable size and is present as a filled sphere. In addition, the metal catalyst has a comparable size to that of the CI and is covered by a graphitic shell. The FFT images of the catalyst (Fig. 1F) and shell part (Fig. 1G) contain diffraction spots with sizes of *ca.* 0.19 nm and 0.33 nm originating from the (200) reflection of metallic Ni (ref. 41) and the (002) reflection of graphite, respectively. A consideration of the sizes and the graphitic layers commonly observed in the CI and the metal catalyst suggests that the CI originates from graphitic carbon formed during the growth of the SWNT. Overall, the CI in PSWNT is an edge-scrolled defect containing few-layer graphene agglomerates nearby PSWNTs.

As CI contributes to a background signal in the absorption spectrum of SWNT batches, understanding its absorption feature is important. As part of a study aimed at generating

purer forms of SWNTs, we found that chloroform serves as a solvent to selectively disperse CIs from PSWNTs. The dispersion is prepared by 20 min sonication of a mixture of PSWNTs (1 mg) and dry chloroform (4 mL) followed by 10 kg centrifugation for 10 min. A photograph displayed in the inset of Fig. 2A shows that the generated dispersion has a pitch-black color. The corresponding UV-vis-MWIR absorption spectrum of CI (Fig. 2A) in the dispersion comprises a featureless curve in the 200–3200 nm range along with a  $\pi$  plasmon band at 261 nm, which originates from the graphitic carbon structure.<sup>42,43</sup> Moreover, the measurement of the FT-IR spectrum and stitching to Fig. 1A (Fig. S1 of ESI†) yields the featureless absorption spectrum up to 8000 nm. Clearly, 5847, 6233, and 7337 nm bands are corresponding to the carbonyl bands (*i.e.*, 1710, 1604, and 1362  $cm^{-1}$ ), phenol, *etc.* (see ESI† for detailed FT-IR assignment), respectively. This result indicates that defects of CI mainly originate from the oxygenated defects.<sup>44–46</sup> The remaining IR features are associated with chloroform. Interestingly, the MWIR spectral region resembles that of graphenes<sup>47,48</sup> rather than that of CB (ref. 49) (see Fig. S2A, S2B, and S2C† for absorption comparison of CI, CB, and graphenes). The concave and converse absorption features of respective CI and CB made a clear distinction. The smooth region in the spectrum of the CI-containing dispersion up to 8000 nm was best-fitted (*i.e.*,  $R^2 = 0.99925$ , Fig. S1†) using a biexponential curve (red):

$$y = A_1 e^{-\frac{x}{b_1}} + A_2 e^{-\frac{x}{b_2}} + y_0 \quad (1)$$

where  $A_1$  and  $A_2$  are the coefficients of each exponential,  $b_1$  and  $b_2$  are the fitting parameters, and  $y_0$  is a constant. The values

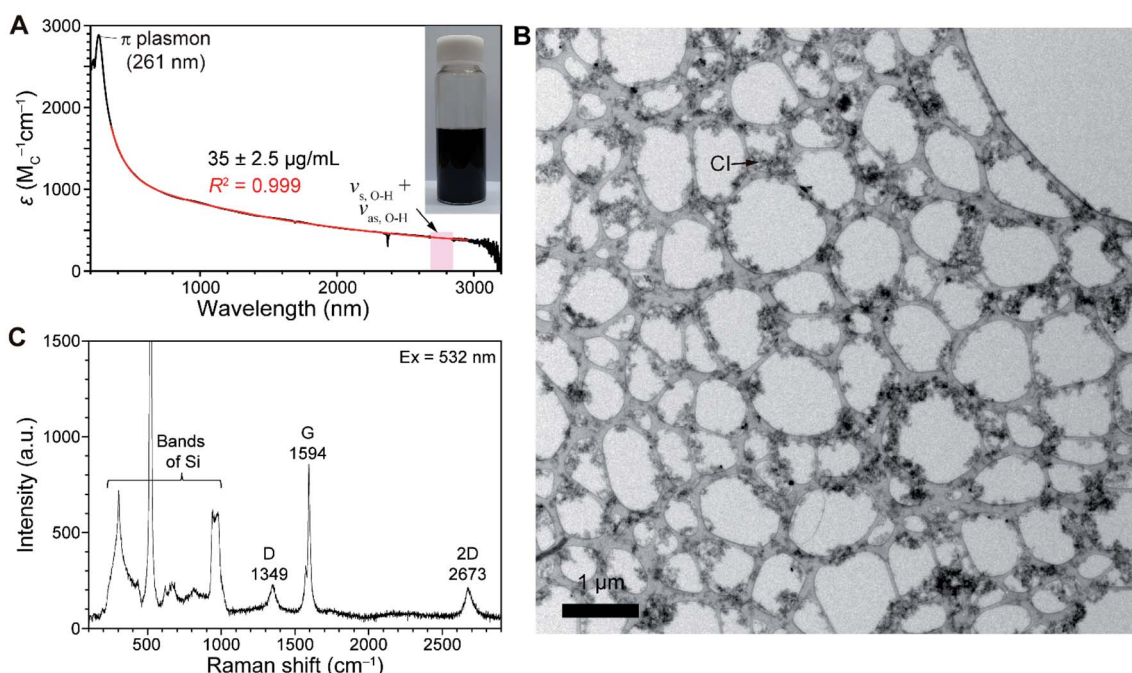


Fig. 2 CI-containing chloroform dispersion of the as-purchased PSWNTs. (A) UV-vis-MWIR absorption spectrum (black) and its biexponential fitting curve (red) of the chloroform dispersion. Shaded area denotes symmetric and asymmetric vibrations of O–H appearing at 2900 nm. Inset: a photograph of the dispersion in chloroform. (B) The corresponding representative TEM image of the dispersion, showing CI agglomerates as major constituents. (C) Raman spectrum of CI deposited on a 285 nm-thick SiO<sub>2</sub>/Si substrate. Raman bands below 1000 cm<sup>-1</sup> originated from Si.



determined for  $A_1$ ,  $A_2$ ,  $b_1$ ,  $b_2$  and  $y_0$  are 1174, 15 055, 1641.9, 110.5, and 186, respectively. These observations along with those arising from TEM studies confirm that the chloroform dispersion consists mainly of CIs. The inspection of TEM images of materials in the chloroform dispersion (Fig. 2B and S3A†) shows that the vast majority of the dispersion comprises CI agglomerates, along with trace amounts of the metal catalyst. The magnified views in additional SEM images of the thick film (Fig. S3D†) supported that selective CI dispersion in chloroform contains massive CIs with few SWNTs.

Studies were carried out to generate exact weight samples of the CI required for determining extinction coefficients ( $\epsilon$ ) in the absorption spectrum. We found that dry CIs can be obtained by filtration of the CI dispersion arising from sonication of 1 mg as-purchased SWNTs in 4 mL chloroform with a filter membrane followed by drying. The dried sample removed from the filter membrane weighing  $35 \pm 2.5 \mu\text{g mL}^{-1}$  has a brittle and cracked film morphology due to its globular particle structure. Using this sample to generate an absorption spectrum (Fig. 2A), we were able to obtain  $\epsilon$  of CI at different wavelengths (e.g., 1170 (carbon  $M$  or  $M_C$ ) $^{-1}$  cm $^{-1}$  at 550 nm). Comparison of absorption cross section ( $\sigma_{\text{abs}}$ ) with monolayer graphenes provides more insights into the nature of CI. Specifically,  $\sigma_{\text{abs}}$  of the CI, determined using the formula  $\sigma_{\text{abs}} = 2.3\epsilon/N_A$ , where  $N_A$  is Avogadro's number ( $6.02 \times 10^{23} \text{ mol}^{-1}$ ), is  $4.47 \times 10^{-18} \text{ cm}^2 \text{ G}^{-1}$  (see ESI† for the detailed calculation). This value is about 76% of the one ( $5.9 \times 10^{-18} \text{ cm}^2$ ) based on 97.7% transmittance of monolayer graphenes.<sup>50</sup> This result indicates that the CI consists of a defective graphene structure.

The Raman spectrum of isolated CI, deposited on a 285 nm-thick  $\text{SiO}_2/\text{Si}$  substrate, was obtained (Fig. 2C). Along with Raman bands originating from Si below 1000 cm $^{-1}$ ,<sup>51</sup> the spectrum produced by excitation at 532 nm exhibits two prominent bands near 1350 cm $^{-1}$  and 1594 cm $^{-1}$  originating from disordered D and graphitic G bands that are commonly observed in graphitic nanocarbon.<sup>52,53</sup> In addition, G band intensities are much stronger than that of the 2D band, suggesting graphitic structures. Moreover, the significant D band intensity indicates a defective graphene structure. However, the spectrum is quite different from those observed for amorphous carbon and CB, which contain larger D bands than G bands, and a concomitant D' band near 1620 cm $^{-1}$ .<sup>53</sup> Based on the intensity ratio of D over G bands ( $I_D/I_G$ ) of the CI (*i.e.*, 0.267) and CB (*i.e.*, 0.87), the defect density  $L_D$  was calculated as 23 and 12 nm, respectively (see ESI† for defect density calculations). This result indicates that the CI has a greater crystalline portion than CB, leading to large contributions in the absorption spectrum.

A plot of optical transitions *vs.*  $d_t$  of the SWNT (Kataura plot<sup>29,30,54</sup> in Fig. 3A) can be employed for determining the reference point to understand the contribution of CIs from the SWNT spectrum. *s*- and *m*-symbols up to 3 nm  $d_t$  were obtained from the respective SDS-encapsulated *s*-SWNT dispersion<sup>29</sup> and Rayleigh measurement of suspended *m*-SWNTs<sup>30</sup> respectively to consider the excitonic effect of SWNTs (see Methods). Therefore, SWNTs with the largest  $d_t$  existing for a given batch was utilized to set the lower bound of optical transition-devoid wavelength region situated above the resulting lowest lying

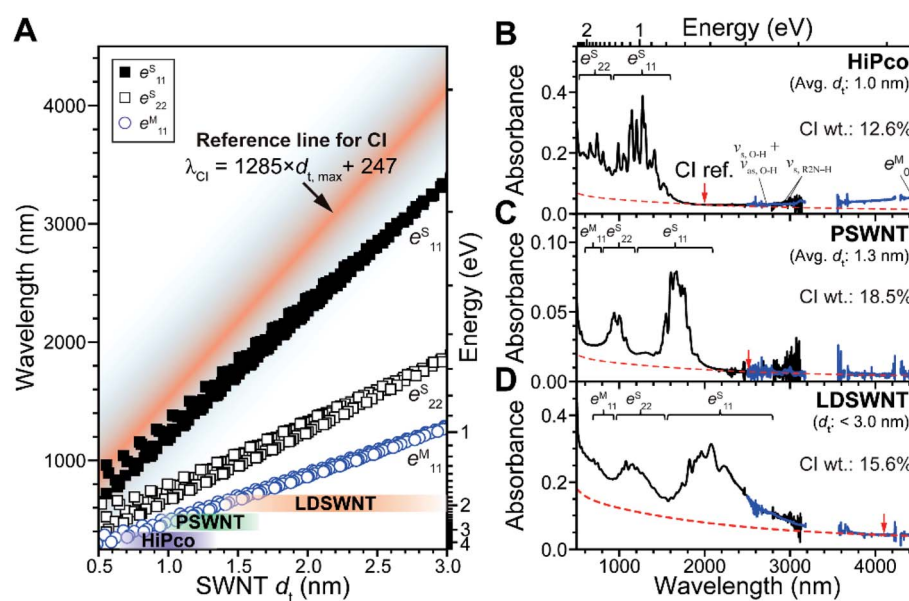


Fig. 3 Quantification of CIs present in SWNT batches with different  $d_t$  ranges. (A) Kataura plot of  $d_t$  vs. optical transition wavelengths based on SDS-wrapped *s*-SWNTs (square) and Rayleigh scattering-based *m*-SWNTs (circle), as reported in the literature.<sup>29,30</sup> Purple, green, and brown areas denote  $d_t$  ranges of each SWNT species. The separation of absorption spectra into SWNT and CI contributions with SWNT batches using the wavelength region containing the least optical transitions corresponding to SWNTs. The absorption spectra of (B) HiPco, (C) PSWNT, and (D) LDSWNT dispersed by FC12 and *p*-xylene in a similar manner. Background absorption of CI is denoted as a dashed curve. Reference points of CI for each SWNT batch were indicated by red arrow. CI reference points of B, C, and D are 1982, 2496, and 4102 nm, respectively, based on eqn (2).



optical transition owing to the inverse relationship between  $d_t$  and optical transitions in energy. This is accomplished by setting a reference point (red line in Fig. 3A) that is distinct from optical transitions of SWNTs with different  $d_t$ , considering full width at half maximum of optical transitions of SWNTs (*i.e.*, 20–30 meV for the first optical transitions ( $e_{11}^s$ ) of *s*-SWNTs<sup>55</sup>) and slight SWNT bundling (*i.e.*, 20–56 meV for the optical transitions for SWNT bundles<sup>56</sup>). Shaded color-coded areas in the plot correspond to SWNT species with different  $d_t$  distributions, in which the quantification of CI is examined. The species, including HiPco process SWNT ( $d_t$  distribution:  $1.0 \pm 0.35$  nm), PSWNT ( $d_t$  distribution:  $1.3 \pm 0.35$  nm), and LDSWNT ( $d_t < 3.0$  nm), were dispersed by sonochemistry using isomolar FC12 (*i.e.*, 0.61 mM) in *p*-xylene and a protocol described in the Methods section. In the Kataura plot, each SWNT with known  $d_t$  distribution has an  $e_{11}^s$  optical transition-devoid wavelength region (red line and above) in the MWIR region, which is used as the CI reference point to determine the net contributions of the SWNT and CI.

The combined results led to empirical derivation of an equation for finding the reference point used for CIs in nm ( $\lambda_{CI}$ ) in correcting various SWNT spectra. The relationship considering the aforementioned full width at half maximum of SWNTs and slight SWNT bundling is as follows:

$$\lambda_{CI} = \alpha d_{t, \max} + \beta \quad (2)$$

where  $\alpha$  and  $\beta$  denote coefficients, and  $d_{t, \max}$  represents the maximum diameter of a given SWNT. The dimensionless coefficient  $\alpha$  is 1285 and  $\beta$  is 247 nm. Using this equation, one can estimate  $\lambda_{CI}$  for a SWNT having known  $d_t$  ranges. The biexponential fitting curve in eqn (1) was utilized to subtract those reference points.

We explored several examples in which this protocol was employed to determine the net spectral contributions of the SWNT and CI. It was reported that a FC12-SWNT dispersion created using aromatic solvents such as *p*-xylene and toluene is enriched in individualized *s*-SWNTs and CIs, and does not contain large amounts of bundled SWNTs.<sup>5,31,55</sup> This fact assures that background absorption in the absorption spectra of the SWNT dispersion mostly originates from CI. The absorption spectrum of the IR region (2500 to 25 000 nm, blue) from FT-IR measurement was stitched in the 2900–3200 nm region of the absorption spectrum acquired using a UV-vis-MWIR absorption spectrometer (black). In the FT-IR region, vibrations originating from surfactants, residual water, and *p*-xylene were also observed (see ESI† for the vibration assignments). At first, bands in the spectra of a PSWNT dispersion (Fig. 3C), whose  $e_{11}^s$  tails up to 2100 nm, are expected not to have *s*-SWNT contributions in the region higher than 2100 nm. Moreover, the  $e_{00}^M$  band, originating from an opened band gap in the density of state continuum caused by SWNT curvature and doping,<sup>57,58</sup> typically occurs in the MWIR region (3000 to 25 000 nm) for *m*-SWNTs with small  $d_t$ . For PSWNTs with a  $d_t$  distribution of  $1.3 \pm 0.35$  nm, 2496 nm was obtained using eqn (2). The resulting subtracted spectrum (Fig. S4†) has nearly no absorbance from 2300 nm.

In a similar manner, contributions of CIs to the spectra of HiPco (Fig. 3B) and LDSWNT (Fig. 3D) dispersions were determined by adjusting the CI spectrum to the reference point in the Kataura plot. HiPco with the smallest  $d_t$  among three SWNT samples was set to have a reference position at 1982 nm and LDSWNTs with the largest  $d_t$  at 4102 nm which is the IR region. Upon closer look, the MWIR region (*i.e.*, 3000–4500 nm) of the HiPco sample displays rising absorption above the CI absorption (red dashed line). This originates from the  $e_{00}^M$  band of *m*-SWNT. Investigation up to long-wavelength and far IR region (8000 to 25 000 nm, Fig. S5†) shows that HiPco and LDSWNT samples exhibit  $e_{00}^M$  while PSWNT does not have. Moreover, HiPco shows maximum of  $e_{00}^M$  at *ca.* 10 000 nm (1000 cm<sup>−1</sup>) while LDSWNT exhibits rising absorption up to 25 000 nm (400 cm<sup>−1</sup>). This clearly indicates that those absorptions depend on the  $d_t$  range of the *m*-SWNT in each sample. This is in line with *m*-SWNT observation using the IR region.<sup>59,60</sup>

By using both of these approaches and the determined  $\varepsilon$  value of CI, we deduced the SWNT concentrations present in various SWNT dispersions. For this, we obtained overall weights in each SWNT dispersion with known absorbance. Separately, the CI concentration was obtained by  $\varepsilon$  using CI reference points for each sample (CI concentration:  $7.19 \pm 0.52$  µg mL<sup>−1</sup> in HiPco dispersion,  $1.93 \pm 0.14$  µg mL<sup>−1</sup> in PSWNT dispersion, and  $15.6 \pm 1.1$  µg mL<sup>−1</sup> in LDSWNT dispersion). The filtration of each dispersion using a 1.0 µm pore-sized PTFE filter followed by complete acetone washing results in the production of films containing both SWNTs and CIs (HiPco:  $49.8 \pm 0.62$  µg mL<sup>−1</sup>; PSWNT:  $8.53 \pm 0.15$  µg mL<sup>−1</sup>; LDSWNT:  $84.1 \pm 1.2$  µg mL<sup>−1</sup>). It is noteworthy that the filtrate did not contain either PSWNTs or CIs. This result indicates that although the absorption spectrum appears to indicate that a small amount of CI is present, it exists in the significantly large weight of 12.6, 18.5, and 15.6% in HiPco, PSWNTs, and LDSWNTs, respectively. Among various SWNT dispersions, HiPco has the smallest CI content, whereas the PSWNT has the largest. The observed increasing CI contributions with the increase in average  $d_t$  in the absorption spectra (Fig. 3B to D) might appear contrasting with the quantified CI weight percentage. However, consideration of both significant *m*-SWNT contents in LDSWNTs and near-absent *m*-SWNT contents in PSWNT explains such CI weight difference.

CI content trends of these SWNTs were confirmed by both SEM and AFM. First, to determine how the morphologies of CI are different for given SWNT batches, SWNT films from each dispersion were prepared by a filtration method. The SEM images (Fig. 4A to C) regardless of the samples display that CIs are much brighter than overall SWNTs. As the *m*-SWNT has much brightness than that of the *s*-SWNT under the SEM image due to higher secondary electrons originating from free electrons,<sup>61</sup> so does metallic CI. Based on this, CI is marked in red, as shown in Fig. 4A' to 4C'. Clearly, CIs in HiPco and LDSWNTs were much conformally bound to the SWNT surface and have a much smaller size (few nm) than that of the PSWNT. Moreover, CIs of the PSWNT are more clustered and much higher contents. This is in line with the determined CI contents in each SWNT batch and the reason why the CI in PSWNT can be



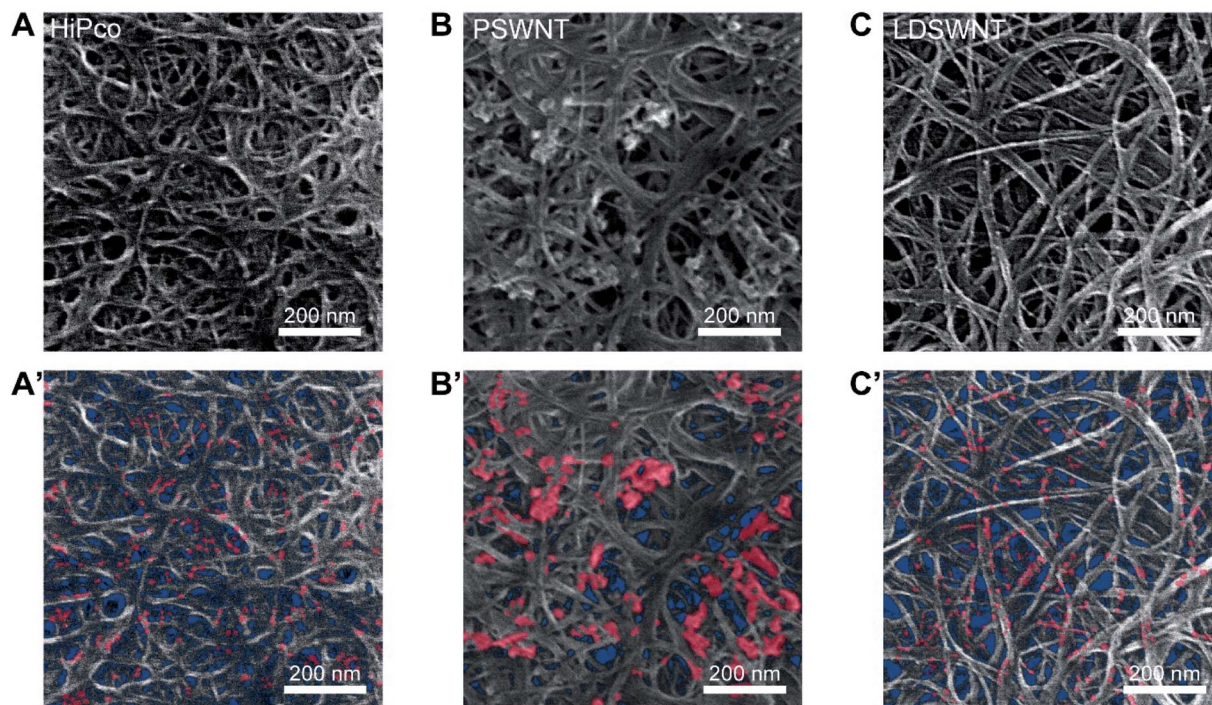


Fig. 4 Visualization in the morphologies of the CI present in each SWNT film. (A to C) SEM images and (A' to C') CI-marked (red) SEM image of each film. The background in the SEM images was colored in blue for visual clarity.

relatively easily removed by chloroform extraction. The AFM results also unequivocally support such proposition. Fig. S6A to S6C<sup>†</sup> show the AFM height images of the respective SWNT deposited on a 285 nm-thick SiO<sub>2</sub>/Si substrate after extensive washing with acetone to remove any residual FC12. Although repetitive washing with acetone, while the PSWNT sample (Fig. S6B<sup>†</sup>) exhibits a smooth individualized SWNT surface and CI according to the previous literature,<sup>31</sup> HiPco (Fig. S6A<sup>†</sup>) shows an irregular height topography on SWNTs along with LDSWNTs to a lesser extent (Fig. S6C<sup>†</sup>), suggesting adsorbed CI. Each growth method of SWNT results in different CI morphologies.

To determine whether chloroform-based CI extraction method can be utilized for the removal of the conformally bound CIs on SWNTs, similar CI extractions for HiPco and LDSWNT samples were conducted. The exfoliation of CIs on those SWNT surfaces requires more vigorous tip sonication with extended time as compared to bath sonication for PSWNTs. The absorption spectra of the resulting CI-enriched dispersion (Fig. S7A and S7B<sup>†</sup>) resemble the biexponential curve of CI of eqn (1) (red), except the overtone (1694 nm) and combination (2371 nm) of chloroform vibrational features.<sup>62,63</sup> The AFM measurement of each extracted CI (inset of Fig. S7A and S7B<sup>†</sup>) shows globular CI morphologies, which are ascribed to the spontaneous graphene scroll in dissimilar solvents.<sup>64,65</sup> This experiment indicates that the CI morphology determines the degree of CI extraction using chloroform.

To confirm the weight percentage measurements, we prepared a bulk sample for TGA. Prior to carrying out this analysis, a FC12-PSWNT dispersion was filtered and washed

with copious amounts of acetone. The result of XPS (Fig. S8A to S8C<sup>†</sup>) confirmed that PSWNTs, acetone-washed PSWNTs and CI samples do not contain appreciable nitrogen contents (*i.e.*, below 0.5%, respectively, Fig. S8D<sup>†</sup>), suggesting that no appreciable flavin surfactant is present in the film. In addition, the increased oxygen content (*i.e.*, 2.0 to 6.2%) at the expense of carbon content (97.5 to 93.3%) for PSWNT/acetone-washed PSWNTs is due to the oxidation of SWNTs and nanocarbons during sonication, whereas the CI displays similar atomic contents with PSWNTs. It is noteworthy that *ca.* 2% of oxygen present in the CI mainly originates from the carbonyl functionality observed in the FT-IR measurement. The results of TGA (Fig. S9A to S9C<sup>†</sup>) show that PSWNTs, CIs, and acetone-washed PSWNTs have different thermograms against air. For instance, while the CI displays a lower decomposition temperature (a maximum weight loss at 600 °C), acetone-washed PSWNTs display a higher decomposition temperature by 40–80 °C (a large weight loss at 640–680 °C). The TGA trace of PSWNTs is in between that of CIs and acetone-washed PSWNTs. Fitting the thermogram from PSWNTs shows that respective contributions from CI and PSWNT of *ca.* 20% and 80% (Fig. S9D<sup>†</sup>) give the closest match with the above-determined weight percentage of CIs in PSWNTs (*i.e.*, 18.5%).

We demonstrated the efficacy of using chloroform to separate CIs from PSWNTs by comparing the produced PSWNT to the as-purchased SPSWNT, which compared to PSWNTs has a 1–3% CI content. For this purpose, the CI was repetitively extracted from PSWNTs using chloroform (see Methods). Fig. 5A to D display the normalized UV-vis-MWIR spectra of FC12-PSWNT dispersions obtained from varying extraction



times (*i.e.*, without extraction, 3 times, and 6 times). While the spectra are not greatly different in terms of intensities of optical transitions and *m/s*-ratios of PSWNTs, it is clear that the CI contribution is lowered by increasing the number of extractions (see dashed lines in Fig. 5A to C). In addition, the chloroform extraction with 6 times results in reduced overall weight by 78% and increased SWNT purity (81 to 91%), as shown in Fig. S10.† Overlaid CI-subtracted net SWNT spectra with varying number of extraction (Fig. S11†) indicate that the spectra remain similar, suggesting a negligible change in PSWNT distribution along with the effective removal of CI. Especially, 3 to 6 times extracted samples have a lower CI level as compared to SPSWNTs, as shown in Fig. 5D. Moreover, comparison of PSWNTs without chloroform extraction and SPSWNTs indicates that there are significant  $e_{11}^S$  and higher transition shifts to a longer wavelength, possibly due to the oxidative instability of the smaller- $d_t$  PSWNT during the CI removal step for SPSWNT preparation. Moreover, SPSWNTs prepared under mild oxidation conditions are about 40 times expensive as compared to PSWNTs.<sup>30</sup>

Those trends were confirmed by AFM height measurements. The corresponding AFM images after acetone treatment (Fig. 5E to G) show that the CI content decreased remarkably after 3 times CI extraction. In addition, as the CI extraction proceeded up to 6 times from as-purchased SWNTs, the average number of CIs per SWNT length (Fig. S12†) continued to decrease (*i.e.*,  $2.17 \pm 0.34$ ,  $0.69 \pm 0.32$  and  $0.32 \pm 0.05$  CI/SWNT length ( $\mu\text{m}$ ) for without extraction, 3 times extracted and 6 times extracted

samples, respectively). This value of the 6 times extracted sample is comparable with that of the SPSWNT sample (0.21 CIs per  $1\text{ }\mu\text{m}$  SWNTs) (Fig. 5H). Comparison between the use of the chloroform extraction and oxidative CI removal methods clearly demonstrates that the former method is facile and it does not greatly disturb the original SWNT distribution.

The effects of CI on  $\sigma$  and  $\kappa$ , two important physical properties of a SWNT, were elucidated. The device used for this purpose contains both pre-patterned  $\sigma$  and  $\kappa$  measuring components (see Fig. S13† for the detailed configuration), enabling simultaneous measurements of thin SWNT films to be made. PSWNT films of varying CI contents were transferred onto an electrode-pre-patterned substrate, as shown in Fig. 6A and S14† (see Methods). A deterministic transfer method was utilized to transfer the thin SWNT film (Fig. 6A), according to the literature.<sup>35</sup> This method consists of the following steps: (i) filtration of SWNT dispersion on a membrane, (ii) transfer of SWNT films to a quartz substrate by dissolution of the membrane, (iii) PMMA spin-coating onto a SWNT film/quartz substrate, (iv) floating PMMA/SWNT films from the quartz substrate by buffered oxide etchants, and (v) transferring onto a desired substrate using two sets of translators and dissolution of the PMMA layer with acetone. Prior to step (iv), the film is cut into a desired size ( $5\text{ mm} \times 3\text{ mm}$ ).

PSWNT dispersions containing different amounts of CI were prepared to determine the effect of weight percentage of CI on  $\sigma$  and  $\kappa$ . FC12-PSWNT dispersions with specific CI weight percentage (*i.e.*, 1.93, 3.86, 9.65, 19.3, and  $38.6\text{ }\mu\text{g mL}^{-1}$  or 18.5,

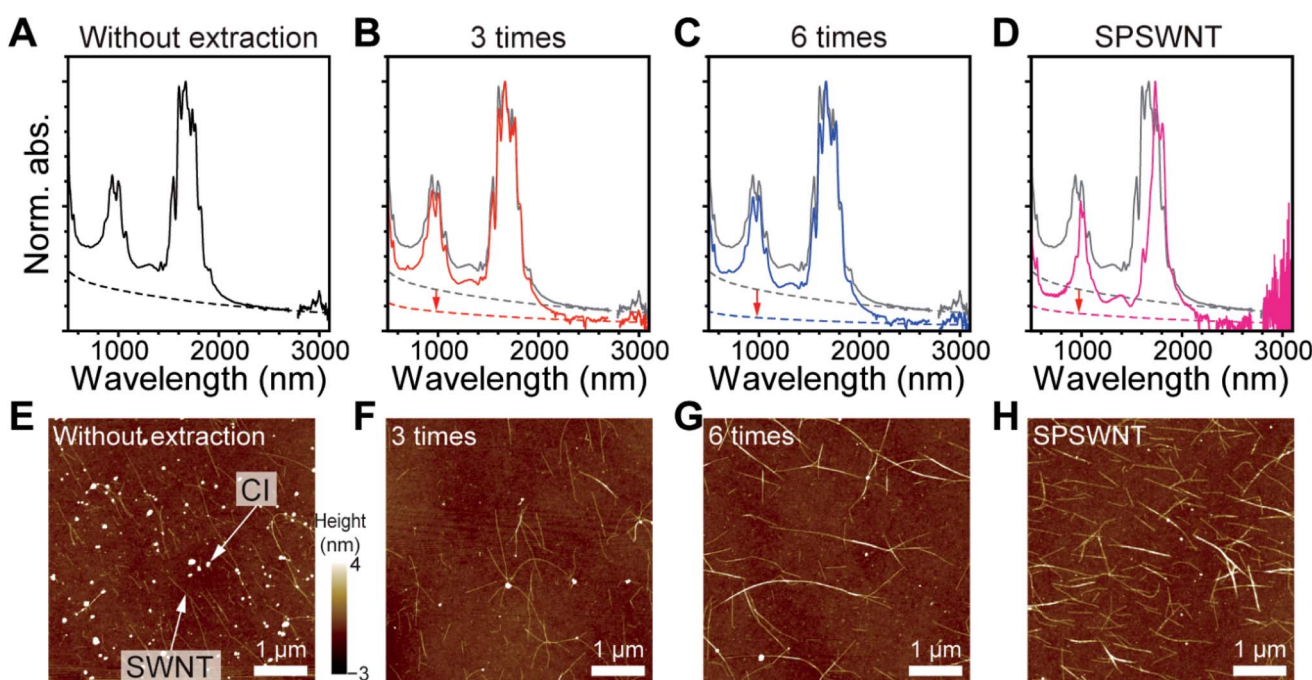


Fig. 5 Effects of repetitive chloroform extraction of PSWNTs on SWNT distribution and degree of CI removal. UV-vis-MWIR absorption spectra from (A) without chloroform extraction (black), (B) 3 times chloroform extraction (red), (C) 6 times chloroform extraction (blue) samples, and (D) SPSWNT dispersion (magenta), which were dispersed by FC12 in *p*-xylene. Dashed lines indicate CI contributions to the spectra. Grey spectra were originating from the sample without chloroform extraction for visual comparison. (E–H) The corresponding AFM height images whose samples were deposited on 285 nm-thick  $\text{SiO}_2/\text{Si}$  substrates. FC12 was completely washed with acetone.



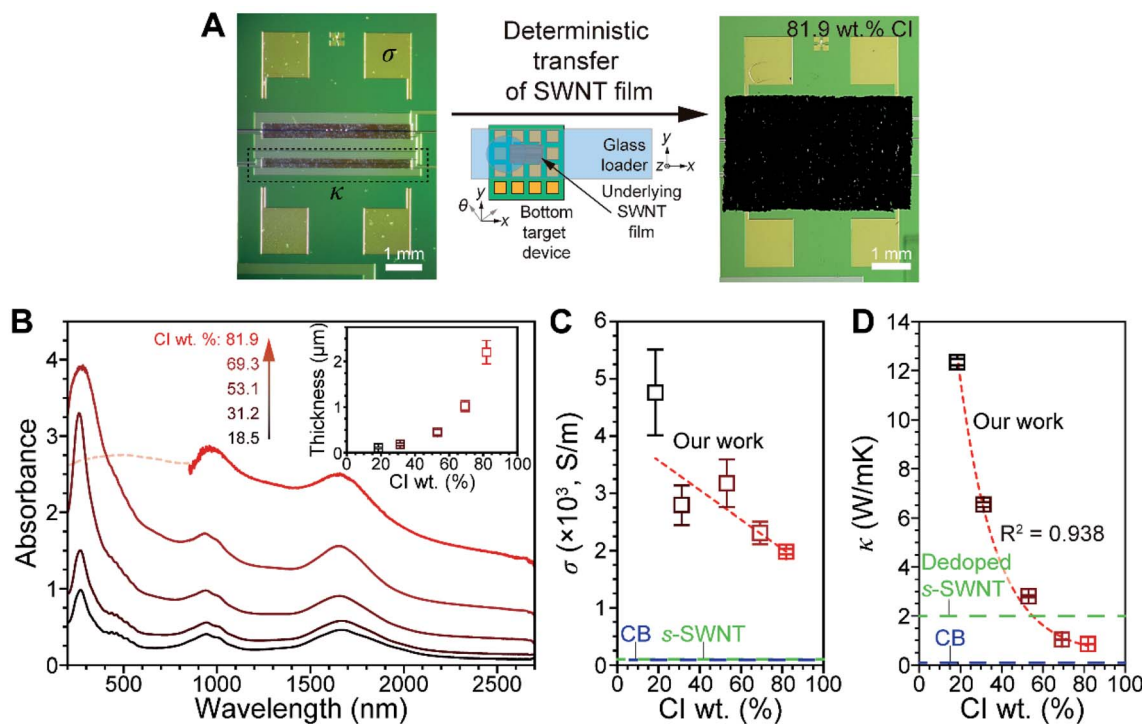


Fig. 6 Effect of Cl contents on the physical properties of a PSWNT film. (A) Schematic of the deterministic transfer of PSWNT films with the largest Cl content. Left and right photographs are before and after the transfer of the PSWNT film. Four Au electrodes were utilized for the  $\sigma$  measurement and the dashed box area is used for the  $\kappa$  measurement. (B) Absorption spectra of PSWNT films with the increase in Cl concentration on quartz. Inset: thickness change of PSWNT films measured using a surface profiler. The error bars for thickness were obtained by averaging the thicknesses of five different areas. Plots of (C)  $\sigma$  and (D)  $\kappa$  vs. Cl weight percentage in PSWNT films, and comparison with CB and s-SWNTs.

31.2, 53.1, 69.3, and 81.9 wt% in carbon) were prepared by adding the Cl-enriched powder to FC12-PSWNT dispersions. Upon increasing the Cl weight percentage in the PSWNT dispersion, background absorption originating from the Cl increases proportionally without changing the optical features of PSWNT (Fig. S15†). The dispersions were subjected to filtration and films were prepared by dissolution of the filtration membrane using acetone vapor to remove FC12 (see Methods). After step (ii) (Fig. 6B), the absorption spectra of the produced PSWNT films were acquired. The spectra contain broad and featureless  $e_{11}^M$ ,  $e_{22}^S$ , and  $e_{11}^S$  bands owing to PSWNT bundling. Separately, the average thickness of each PSWNT film was varied from 104 to 2201 nm with the films having increasing roughness (Fig. S16A to S16E† for each height profile).

The  $\sigma$  and  $\kappa$  values of PSWNT films containing varying Cl weight percentages (Fig. 6C and D) were obtained under vacuum conditions (*i.e.*,  $7.5 \times 10^{-6}$  torr). Plots of  $\sigma$  and  $\kappa$  vs. Cl weight percentage show that both values decrease with the increase in Cl weight percentage. For instance,  $\sigma$  values decrease from  $4800$  to  $2000$   $S\ m^{-1}$  as the Cl weight percentage increases. These values lie in between those of purified *m*-SWNT (*i.e.*,  $5 \times 10^4$   $S\ m^{-1}$ ) and *s*-SWNT (*i.e.*,  $100$   $S\ m^{-1}$ ) films,<sup>66</sup> and are much greater than that of CB (*i.e.*,  $90$   $S\ m^{-1}$ ).<sup>67</sup> It is reasonable that the sample with the highest Cl weight percentage shows greater  $\sigma$  than that of CB since Cl has less defects. In addition,  $\kappa$  values decrease from  $12$  to  $0.8$   $W\ mK^{-1}$  with the increase in Cl

weight percentage, and they are much smaller than  $\kappa$  of *m*-SWNT ( $100\ W\ mK^{-1}$ ) and *s*-SWNT ( $200\ W\ mK^{-1}$ ) films.<sup>68</sup> Interestingly,  $\kappa$  undergoes a greater change than does  $\sigma$  with the increase in Cl weight percentage.

Empirically, the Wiedemann–Franz law<sup>69</sup> suggests that the ratio of  $\kappa$  to  $\sigma$  of a metal is proportional to the temperature according to  $\kappa/\sigma = LT$ , where  $L$  is the Lorenz number ( $2.44 \times 10^{-8}\ W\Omega K^{-2}$ ). In our case, samples with 18.5–81.9 wt% Cl display  $\kappa/\sigma$  from  $2.71 \times 10^{-3}$  to  $5 \times 10^{-4}\ W\Omega K^{-1}$  at room temperature. With the increase in Cl weight percentage, their  $LT$  value ( $7.27 \times 10^{-6}\ W\Omega K^{-1}$ ) approached that of the metal. The deviation likely originates from electrical transport variations from *s*-PSWNT to Cl as a major conduction channel. Nevertheless, this result suggests that the Cl has a metallic nature. In addition, respective  $\kappa$  values of CB and dedoped *s*-SWNT are  $0.1$ – $0.2\ W\ mK^{-1}$  (ref. 70 and 71) and  $2\ W\ mK^{-1}$ ,<sup>8</sup> and the Cl value ( $0.80\ W\ mK^{-1}$  for 81.9 wt% Cl) lies between both. The  $\kappa$  value in the Cl and CB also follows a defect trend, as observed in the absorption and Raman results.

## 4. Conclusions

As described above, we developed techniques for the removal and quantification of Cl present in a PSWNT batch. PSWNT contains bundled SWNTs, Cls and a metal catalyst. We found that sonochemical dispersion of PSWNTs in chloroform



selectively disperses CI. The produced CI is an agglomerated form of edge-scrolled and defective few-layer graphene with a lateral size of 10–20 nm. UV-vis-MWIR absorption spectroscopic analysis of the CI shows that its absorption profile can be fitted by a biexponential curve and that it has an absorption cross section comparable to that of graphenes. Through a consideration of a Kataura plot and CI absorption, we were able to construct the net SWNT spectrum by using reference points in the MWIR region to subtract the CI contribution according to a given SWNT  $d_t$  distribution, which differs in different SWNT batches. The quantification method of CI was verified using SEM and AFM methodologies. The extension of absorption measurement up to far IR enables the measurement of the accurate contribution of  $s$ - and  $m$ -SWNTs. The efficacy of repetitive CI removal using a chloroform extraction was assessed and compared to the oxidative removal of CIs. The results indicate that the chloroform extraction is a much milder process. While the CI weight percentage in the SWNT film varies from 18.5 to 82%, the electrical conductivity of the SWNT varies from 4800 to 2000 S m<sup>-1</sup>, whereas thermal conductivities vary from 12 to 0.8 W mK<sup>-1</sup>. The morphological and optoelectronic properties of CI elucidated in this investigation provide a complete picture of an important factor governing the electronic properties of a SWNT.

## Author contributions

S. J. conceived the idea, analyzed the data and wrote the manuscript. M. P. performed the FC12 synthesis, SWNT dispersion, CI enrichments and main characterizations. I. C. helped to prepare SWNT dispersions.

## Conflicts of interest

There is no conflict of interest.

## Acknowledgements

This research was mainly supported by the Basic Science Research Program through the National Research Foundation of Korea (NRF) funded by the Ministry of Education, Science, and Technology (2022R1A2C1006932 and 2020R1A4A1017737).

## References

- 1 J. Wu, L. Xie, G. Hong, H. E. Lim, B. Thendie, Y. Miyata, H. Shinohara and H. Dai, *Nano Res.*, 2012, **5**, 388–394.
- 2 L. S. Liyanage, H. Lee, N. Patil, S. Park, S. Mitra, Z. Bao and H.-S. P. Wong, *ACS Nano*, 2012, **6**, 451–458.
- 3 G. J. Brady, Y. Joo, M.-Y. Wu, M. J. Shea, P. Gopalan and M. S. Arnold, *ACS Nano*, 2014, **8**, 11614–11621.
- 4 J. Ding, Z. Li, J. Lefebvre, F. Cheng, G. Dubey, S. Zou, P. Finnie, A. Hrdina, L. Scoles, G. P. Lopinski, C. T. Kingston, B. Simard and P. R. L. Malenfant, *Nanoscale*, 2014, **6**, 2328–2339.
- 5 M. Park, S. Kim, H. Kwon, S. Hong, S. Im and S.-Y. Ju, *ACS Appl. Mater. Interfaces*, 2016, **8**, 23270–23280.
- 6 Y. Nonoguchi, K. Ohashi, R. Kanazawa, K. Ashiba, K. Hata, T. Nakagawa, C. Adachi, T. Tanase and T. Kawai, *Sci. Rep.*, 2013, **3**, 3344.
- 7 C.-K. Mai, B. Russ, S. L. Fronk, N. Hu, M. B. Chan-Park, J. J. Urban, R. A. Segalman, M. L. Chabinyc and G. C. Bazan, *Energy Environ. Sci.*, 2015, **8**, 2341–2346.
- 8 A. D. Avery, B. H. Zhou, J. Lee, E.-S. Lee, E. M. Miller, R. Ihly, D. Wesenberg, K. S. Mistry, S. L. Guillot, B. L. Zink, Y.-H. Kim, J. L. Blackburn and A. J. Ferguson, *Nat. Energy*, 2016, **1**, 16033.
- 9 E. Kymakis and G. A. J. Amaralunga, *Appl. Phys. Lett.*, 2002, **80**, 112–114.
- 10 E. Kymakis, I. Alexandrou and G. A. J. Amaralunga, *J. Appl. Phys.*, 2003, **93**, 1764–1768.
- 11 R. V. Salvatierra, C. E. Cava, L. S. Roman and A. J. G. Zarbin, *Adv. Funct. Mater.*, 2013, **23**, 1490–1499.
- 12 C. Journet, W. K. Maser, P. Bernier, A. Loiseau, M. L. de la Chapelle, S. Lefrant, P. Deniard, R. Lee and J. E. Fischer, *Nature*, 1997, **388**, 756–758.
- 13 B. Bendjemil, E. Borowiak-Palen, A. Graff, T. Pichler, M. Guerioune, J. Fink and M. Knupfer, *Appl. Phys. A*, 2004, **78**, 311–314.
- 14 S. Yasuda, T. Hiraoka, D. N. Futaba, T. Yamada, M. Yumura and K. Hata, *Nano Lett.*, 2009, **9**, 769–773.
- 15 N. Matsumoto, G. Chen, M. Yumura, D. N. Futaba and K. Hata, *Nanoscale*, 2015, **7**, 5126–5133.
- 16 D. Vilela, A. Ansón-Casaos, M. T. Martínez, M. C. González and A. Escarpa, *Lab Chip*, 2012, **12**, 2006–2014.
- 17 Raymor, *PlasmaTubes Single-Wall Carbon Nanotubes – SWCNT | Raymor – Nanotubes for Electronics*, <https://raymor.com/our-products/plasmatubes/>, (accessed 2021/10/20, 2021).
- 18 S. Ghosh, S. M. Bachilo, R. A. Simonette, K. M. Beckingham and R. B. Weisman, *Science*, 2010, **330**, 1656.
- 19 M. S. Arnold, A. A. Green, J. F. Hulvat, S. I. Stupp and M. C. Hersam, *Nat. Nanotechnol.*, 2006, **1**, 60–65.
- 20 C. Y. Khrapin, J. A. Fagan and M. Zheng, *J. Am. Chem. Soc.*, 2013, **135**, 6822–6825.
- 21 H. Liu, D. Nishide, T. Tanaka and H. Kataura, *Nat. Commun.*, 2011, **2**, 309.
- 22 A. Nish, J.-Y. Hwang, J. Doig and R. J. Nicholas, *Nat. Nanotechnol.*, 2007, **2**, 640–646.
- 23 S. Bandow, S. Asaka, X. Zhao and Y. Ando, *Appl. Phys. A*, 1998, **67**, 23–27.
- 24 J. L. Zimmerman, R. K. Bradley, C. B. Huffman, R. H. Hauge and J. L. Margrave, *Chem. Mater.*, 2000, **12**, 1361–1366.
- 25 A. C. Dillon, T. Gennett, K. M. Jones, J. L. Alleman, P. A. Parilla and M. J. Heben, *Adv. Mater.*, 1999, **11**, 1354–1358.
- 26 Z. Li, J. Ding, P. Finnie, J. Lefebvre, F. Cheng, C. T. Kingston and P. R. L. Malenfant, *Nano Res.*, 2015, **8**, 2179–2187.
- 27 J. Wang, T. D. Nguyen, Q. Cao, Y. Wang, M. Y. C. Tan and M. B. Chan-Park, *ACS Nano*, 2016, **10**, 3222–3232.
- 28 E. Koo and S.-Y. Ju, *Carbon*, 2015, **86**, 318–324.
- 29 R. B. Weisman and S. M. Bachilo, *Nano Lett.*, 2003, **3**, 1235–1238.



30 K. Liu, J. Deslippe, F. Xiao, R. B. Capaz, X. Hong, S. Aloni, A. Zettl, W. Wang, X. Bai, S. G. Louie, E. Wang and F. Wang, *Nat. Nanotechnol.*, 2012, **7**, 325–329.

31 I.-S. Choi, M. Park, E. Koo and S.-Y. Ju, *Carbon*, 2021, **184**, 346–356.

32 J. Deslippe, C. D. Spataru, D. Prendergast and S. G. Louie, *Nano Lett.*, 2007, **7**, 1626–1630.

33 F. Wang, G. Dukovic, E. Brus Louis and F. Heinz Tony, *Science*, 2005, **308**, 838–841.

34 A. Reina, H. Son, L. Jiao, B. Fan, M. S. Dresselhaus, Z. Liu and J. Kong, *J. Phys. Chem. C*, 2008, **112**, 17741–17744.

35 M. Park and S.-Y. Ju, *Bull. Korean Chem. Soc.*, 2022, **43**, 196–200.

36 V. Linseis, F. Völklein, H. Reith, K. Nielsch and P. Woias, *Rev. Sci. Instrum.*, 2018, **89**, 015110.

37 M. Pawlyta, J.-N. Rouzaud and S. Duber, *Carbon*, 2015, **84**, 479–490.

38 C. T. Wirth, S. Hofmann and J. Robertson, *Diamond Relat. Mater.*, 2009, **18**, 940–945.

39 B. Aleman, R. Ranchoral, V. Reguero, B. Mas and J. J. Vilatela, *J. Mater. Chem. C*, 2017, **5**, 5544–5550.

40 O. Akbarzadeh, N. A. Mohd Zabidi, Y. Abdul Wahab, N. A. Hamizi, Z. Z. Chowdhury, Z. Merican Aljunid Merican, M. Ab Rahman, S. Akhter, E. Rasouli and M. R. Johan, *Symmetry*, 2018, **10**, 572.

41 S. Hofmann, R. Sharma, C. Ducati, G. Du, C. Mattevi, C. Cepek, M. Cantoro, S. Pisana, A. Parvez, F. Cervantes-Sodi, A. C. Ferrari, R. Dunin-Borkowski, S. Lizzit, L. Petaccia, A. Goldoni and J. Robertson, *Nano Lett.*, 2007, **7**, 602–608.

42 K. L. Day and D. R. Huffman, *Nat. Phys. Sci.*, 1973, **243**, 50–51.

43 A. V. Naumov, S. Ghosh, D. A. Tsyboulski, S. M. Bachilo and R. B. Weisman, *ACS Nano*, 2011, **5**, 1639–1648.

44 A. Kuznetsova, I. Popova, J. T. Yates, M. J. Bronikowski, C. B. Huffman, J. Liu, R. E. Smalley, H. H. Hwu and J. G. Chen, *J. Am. Chem. Soc.*, 2001, **123**, 10699–10704.

45 J. Zhang, H. Zou, Q. Qing, Y. Yang, Q. Li, Z. Liu, X. Guo and Z. Du, *J. Phys. Chem. B*, 2003, **107**, 3712–3718.

46 U. J. Kim, C. A. Furtado, X. Liu, G. Chen and P. C. Eklund, *J. Am. Chem. Soc.*, 2005, **127**, 15437–15445.

47 K. F. Mak, J. Shan and T. F. Heinz, *Phys. Rev. Lett.*, 2011, **106**, 046401.

48 S. Villar-Rodil, J. I. Paredes, A. Martínez-Alonso and J. M. D. Tascón, *J. Mater. Chem.*, 2009, **19**, 3591–3593.

49 B. Zhao, M. E. Itkis, S. Niyogi, H. Hu, J. Zhang and R. C. Haddon, *J. Phys. Chem. B*, 2004, **108**, 8136–8141.

50 R. R. Nair, P. Blake, A. N. Grigorenko, K. S. Novoselov, T. J. Booth, T. Stauber, N. M. R. Peres and A. K. Geim, *Science*, 2008, **320**, 1308.

51 D. M. Zhigunov, G. N. Kamaev, P. K. Kashkarov and V. A. Volodin, *Appl. Phys. Lett.*, 2018, **113**, 023101.

52 M. S. Dresselhaus, A. Jorio, A. G. Souza Filho and R. Saito, *Philos. Trans. R. Soc., A*, 2010, **368**, 5355–5377.

53 L. M. Malard, M. A. Pimenta, G. Dresselhaus and M. S. Dresselhaus, *Phys. Rep.*, 2009, **473**, 51–87.

54 H. Kataura, Y. Kumazawa, Y. Maniwa, I. Umezu, S. Suzuki, Y. Ohtsuka and Y. Achiba, *Synth. Met.*, 1999, **103**, 2555–2558.

55 S.-Y. Ju, W. P. Kopcha and F. Papadimitrakopoulos, *Science*, 2009, **323**, 1319–1323.

56 F. Wang, M. Y. Sfeir, L. Huang, X. M. H. Huang, Y. Wu, J. Kim, J. Hone, S. O'Brien, L. E. Brus and T. F. Heinz, *Phys. Rev. Lett.*, 2006, **96**, 167401.

57 Z. Xu, W. Lu, W. Wang, C. Gu, K. Liu, X. Bai, E. Wang and H. Dai, *Adv. Mater.*, 2008, **20**, 3615–3619.

58 A. K. Manna and S. K. Pati, *Nanoscale*, 2010, **2**, 1190–1195.

59 M. E. Itkis, D. E. Perea, S. Niyogi, S. M. Rickard, M. A. Hamon, H. Hu, B. Zhao and R. C. Haddon, *Nano Lett.*, 2003, **3**, 309–314.

60 K. Oi, J. Komoto, T. Kawai and Y. Nonoguchi, *Synth. Met.*, 2021, **282**, 116958.

61 J. Li, Y. He, Y. Han, K. Liu, J. Wang, Q. Li, S. Fan and K. Jiang, *Nano Lett.*, 2012, **12**, 4095–4101.

62 T. G. Gibian and D. S. McKinney, *J. Am. Chem. Soc.*, 1951, **73**, 1431–1434.

63 D. Kurzydłowski, T. Chumak and J. Rogoża, *Crystals*, 2020, **10**, 920.

64 U. Mirsaidov, V. R. S. S. Mokkapati, D. Bhattacharya, H. Andersen, M. Bosman, B. Özyilmaz and P. Matsudaira, *Lab Chip*, 2013, **13**, 2874–2878.

65 X. Xie, L. Ju, X. Feng, Y. Sun, R. Zhou, K. Liu, S. Fan, Q. Li and K. Jiang, *Nano Lett.*, 2009, **9**, 2565–2570.

66 K. Yanagi, H. Udoguchi, S. Sagitani, Y. Oshima, T. Takenobu, H. Kataura, T. Ishida, K. Matsuda and Y. Maniwa, *ACS Nano*, 2010, **4**, 4027–4032.

67 B. Marinho, M. Ghislandi, E. Tkalya, C. E. Koning and G. de With, *Powder Technol.*, 2012, **221**, 351–358.

68 F. Lian, J. P. Llinas, Z. Li, D. Estrada and E. Pop, *Appl. Phys. Lett.*, 2016, **108**, 103101.

69 N. Lu, L. Li, N. Gao and M. Liu, *J. Appl. Phys.*, 2016, **120**, 195108.

70 W. R. Smith and G. B. Wilkes, *Ind. Eng. Chem.*, 1944, **36**, 1111–1112.

71 P. E. Khizhnyak, A. V. Chechetkin and A. P. Glybin, *J. Eng. Phys.*, 1979, **37**, 1073–1075.

